

Change Detection Based on Pulse-Coupled Neural Networks and the NMI Feature for High Spatial Resolution Remote Sensing Imagery

Yanfei Zhong, *Member, IEEE*, Wenfeng Liu, Ji Zhao, and Liangpei Zhang, *Senior Member, IEEE*

Abstract—In this letter, a change detection algorithm based on pulse-coupled neural networks (PCNN) and the normalized moment of inertia (NMI) feature is proposed for high spatial resolution (HSR) remote sensing imagery. To better analyze a large remote sensing image, the whole image is divided into blocks by the use of a deblocking mechanism. The PCNN model is utilized to obtain the initial binary image, and the NMI feature is calculated based on the binary image to detect the hot spot changed areas. Finally, the changed areas are processed by expectation–maximization to obtain the final change map. The experimental results using QuickBird and IKONOS images demonstrate that the proposed algorithm has the ability to provide better change detection results for HSR images than the traditional PCNN change detection algorithms.

Index Terms—Change detection, high spatial resolution (HSR) imagery, normalized moment of inertia (NMI) feature, pulse-coupled neural networks (PCNN), remote sensing.

I. INTRODUCTION

CHANGE detection is a key process in many applications utilizing remote sensing images, and it is the process that leads to the identification of change that has occurred on the Earth’s surface by jointly processing two (or more) images acquired from the same geographical area at different times [1]. The accurate change detection of remote sensing images has a wide range of uses, including land use/cover change monitoring, urban growth studies, risk assessment, and environmental investigation [2]. With the increasing availability of high spatial resolution (HSR) remote sensing images (e.g., IKONOS and QuickBird) covering the same geographical area, it is possible to identify detailed changes occurring at the level of ground structures such as buildings [1]. In the remote sensing field, a variety of different change detection algorithms have been designed and proposed in the past, such as image differencing [3], change vector analysis [4], principal component analysis [5],

Manuscript received May 17, 2014; revised July 9, 2014; accepted August 3, 2014. This work was supported in part by the National Natural Science Foundation of China under Grant 41371344, by the Foundation for the Author of National Excellent Doctoral Dissertation of the People’s Republic of China (FANEDD) under Grant 201052, and by the Fundamental Research Funds for the Central Universities under Grant 2042014kf00231.

The authors are with the State Key Laboratory of Information Engineering in Surveying, Mapping and Remote Sensing, Wuhan University, Wuhan 430079, China (e-mail: zhongyanfei@whu.edu.cn; liufeng4652177@163.com; zhaobj2015@gmail.com; zlp62@whu.edu.cn).

Color versions of one or more of the figures in this paper are available online at <http://ieeexplore.ieee.org>.

Digital Object Identifier 10.1109/LGRS.2014.2349937

and the expectation–maximization (EM) algorithm [6]. These previous studies have mainly focused on low and medium spatial resolution images. In contrast, HSR remote sensing images have more spatial details (e.g., shapes of buildings), and the spatial relations between adjacent pixels are particularly important. Spatial-context-based change detection algorithms [7], the GeoCDX system [8], and neural network algorithms [9], [10] have also been proposed for use with HSR images.

For HSR remote sensing imagery, new problems due to the sheer amount of data need to be solved. In [11], a novel approach based on pulse-coupled neural networks [12], [13] for image change detection (PCNNCD) was proposed. PCNN is a relatively new technique that is based on the implementation of the mechanisms underlying the visual cortex of small mammals [12] and has already been applied in many different fields [14]–[16], such as image segmentation [17], [18], satellite image segmentation [19], texture retrieval [20], image fusion [21], and change detection [22]. In PCNNCD, the whole HSR image is divided into many small scenes, and the “hot spot changed areas” (areas of an image where a significant change occurred) are detected by measuring the similarity between the PCNN signal associated with the former image and the one associated with the latter. The experimental results show that this approach is appropriate for change detection, due to the fact that it is context sensitive and lends itself to object analysis. In addition, the “hot spot area” is the whole changed area; that is, all the pixels in the “hot spot area” are considered as the changed pixels, which can result in important detailed information of the area being lost.

In this letter, a modified PCNN change detection algorithm (MPCNNCD) is proposed by combining PCNN with the normalized moment of inertia (NMI) feature for HSR imagery. In MPCNNCD, a deblocking mechanism [23] is used to overlap between different blocks (scenes) to overcome the problem of the whole hot spot changed area. To better detect the hot spot changed areas, a new correlation method based on the NMI feature is proposed, in which the NMI feature can be extracted from a binary PCNN image. Furthermore, the NMI feature is easy to obtain and is invariant to scale, shift, or rotation [24]. Finally, for the detected hot spot changed areas, the EM algorithm is utilized to get the final detailed change map for the hot spot areas.

This letter is organized as follows. Section II briefly describes the background of PCNN and change detection and details the proposed MPCNNCD. Section III presents the qualitative and quantitative experimental results, and Section IV concludes this letter.

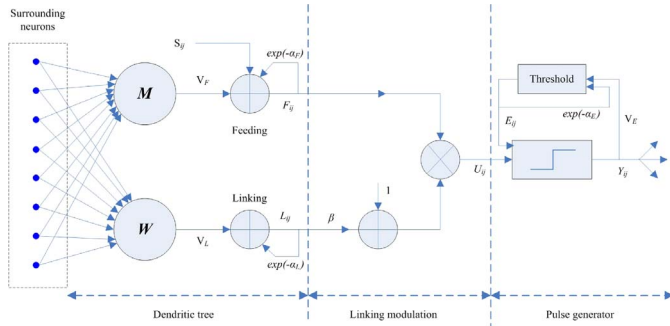


Fig. 1. Structure of the PCNN.

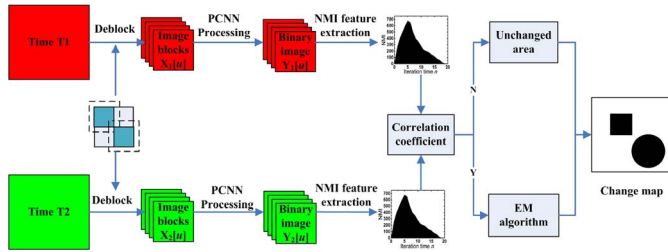


Fig. 2. Flowchart of MPCNNCD.

II. CHANGE DETECTION BASED ON PCNN AND THE NMI FEATURE FOR HSR IMAGERY

In this letter, a modified change detection algorithm based on PCNN and the NMI feature (MPCNNCD) is proposed for HSR remote sensing imagery. PCNN is a biologically inspired neural network [12], which differs from the general artificial neural networks in having only a single layer formed by a 2-D array of laterally linked pulse-coupled neurons, and does not require any training. The relationship between image pixels and the network neurons is a one-to-one correspondence [17], [18]. In the standard PCNN model, the PCNN neuron consists of three parts: the dendritic tree, the linking modulation, and the pulse generator, as shown in Fig. 1 [15]. The role of the dendritic tree is to receive the inputs from two kinds of receptive fields. Depending on the type of receptive field, it is subdivided into two channels (the linking and the feeding). The linking receives a local stimulus from the output of the surrounding neurons, whereas the feeding, as well as the local stimulus, still receives an external stimulus [21].

It has been proved that the time signature by PCNN is invariant to geometrical changes due to the viewing aspect, translation, scale, rotation, and scene illumination [13]. To utilize these features and improve the change detection accuracy, the proposed MPCNNCD combines PCNN and the NMI feature to perform the task of change detection for HSR imagery. The flowchart of MPCNNCD is shown in Fig. 2, and the steps are as follows.

A. Deblocking Mechanism for HSR Images

In order to obtain the change map, a deblocking mechanism [23] is employed for the high-resolution remote sensing images. Because the inconsistent results may appear at the edge areas between different blocks in the original PCNNCD algorithm [11], this study uses an overlap between the different blocks to overcome this problem, i.e., the deblocking mechanism. The proposed algorithm deals with a larger part of the image, then crops the central part and uses it as the result.

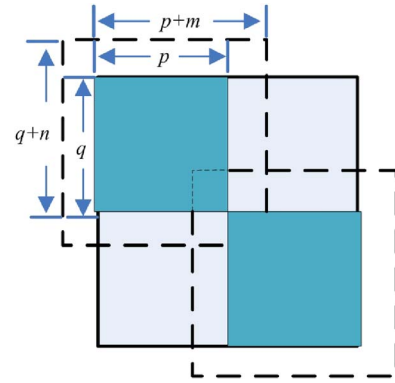


Fig. 3. Deblocking mechanism.

In Fig. 3, the area inside the solid line is saved as the output result. The following steps are based on these blocks. Assuming that the size of an image T1 is $P \times Q$ and the block size is $p \times q$, when dealing with the blocks by adopting the deblocking mechanism, the real processing part is $(p + 2m) \times (q + 2n)$, where m and n are greater than 0. After this step, the original images at the different times, i.e., T1 and T2, will have been divided into many blocks, i.e., $X_1[u]$ and $X_2[u]$, and $u = 1, \dots, U_X$, where U_X represents the number of blocks. These blocks are then processed by PCNN.

B. Initialization of MPCNNCD

The initialization stage can be thought of as a data preprocessing stage. The PCNN model is described as follows [16]:

$$F_{ij}[n] = e^{-\alpha_F} F_{ij}[n-1] + V_F \sum_{kl} M_{ijkl} Y_{kl}[n-1] + S_{ij} \quad (1)$$

$$L_{ij}[n] = e^{-\alpha_L} L_{ij}[n-1] + V_L \sum_{kl} W_{ijkl} Y_{kl}[n-1] \quad (2)$$

$$U_{ij}[n] = F_{ij}[n](1 + \beta L_{ij}[n]) \quad (3)$$

$$Y_{ij}[n] = \begin{cases} 1, & \text{if } U_{ij}[n] > E_{ij}[n-1] \\ 0, & \text{otherwise} \end{cases} \quad (4)$$

$$E_{ij}[n] = e^{-\alpha_E} E_{ij}[n-1] + V_E Y_{ij}[n] \quad (5)$$

where the indices i and j refer to the pixel location in the image or the block, k and l refer to the dislocation in a symmetric neighborhood around one pixel, and n denotes the current iteration (discrete time step), which ranges from 1 to N (N is the total number of iterations). The dendritic tree is given by (1) and (2). The two main components F and L are called feeding and linking, respectively. w_{ijkl} and m_{ijkl} are the synaptic weight coefficients, and S is the external stimulus. V_F and V_L are the normalizing constants. α_F and α_L are the time constants, and generally, $\alpha_F < \alpha_L$. The linking modulation is given in (3), where $U_{ij}[n]$ is the internal state of the neuron. β is the linking parameter, and the pulse generator determines the firing events in the model in (4). $Y_{ij}[n]$ depends on the internal state and threshold. The dynamic threshold of the neuron is (5), where V_E and α_E are the normalized constant and time constant, respectively. A detailed description of the implementation of the standard PCNN model and the functions of these parameters can be found in [14]–[16].

In (1)–(5), matrices F , L , U , E , and Y are all initialized as a zero matrix in the first iteration. Matrix S represents the input image. Each element in matrix S is the digital number value of the pixel.

C. PCNN Processing

After the initialization of MPCNNCD, the next step is the iteration of the proposed algorithm. The algorithm is iteratively executed by computing (1)–(5) until the stopping condition is met, i.e., the user-defined iteration number. In this step, the initial binary images for all the blocks at different times, i.e., $Y_1 = \{Y_1[u], u = 1, \dots, U_X\}$ and $Y_2 = \{Y_2[u], u = 1, \dots, U_X\}$, are obtained by the use of (4) in the PCNN model, where U_X represents the number of blocks.

D. Hot Spot Area Detection Based on NMI Feature Extraction

In the original PCNNCD, the average time signatures are utilized to detect the hot spot areas, as follows [11]:

$$G[u][n] = \frac{\sum_{ij} Y_{ij}[n]}{p \times q}, \quad 1 \leq i \leq p; \quad 1 \leq j \leq q \quad (6)$$

where p and q represent the numbers of rows and columns, respectively. In PCNNCD [11], for the u th block at times T1 and T2, $G_1[u] = \{G_1[u][n]\}$, $G_2[u] = \{G_2[u][n]\}$, and the correlation values are calculated to detect the changed and unchanged areas. It should be noted that the average of the time signatures, i.e., $G[u][n]$, is the average number of neurons that are activated in each iteration, and it does not indicate the detailed distribution. That is, $G[u][n]$ may be the same or similar for different binary images.

To solve this problem, in MPCNNCD, the correlation values between the different blocks at different times are calculated by the NMI feature [24], which is the normalized form of the moment of inertia. The moment of inertia considers the mass distribution to calculate the inertia of a rotating object by the formula $J = \sum_{i=1}^N m_i r_i^2$. m_i is the i th mass of the object with N mass in total, which can be equal to the value of the intensity of a pixel, considering the pixel as a particle for a gray image. r_i represents the distance from the axis of rotation. The moment of inertia is therefore invariant to translation and rotation, depending on the position of the axis of rotation and on the mass of the rotating object. For the binary image obtained by the PCNN processing step, the moment of inertia around the gravity center (i_g, j_g) is

$$J_{i_g j_g} = \sum_{i=1}^p \sum_{j=1}^q [(i - i_g)^2 + (j - j_g)^2] Y_{ij} \quad (7)$$

$$i_g = \frac{\sum_{i=1}^p \sum_{j=1}^q i \times Y_{ij}}{\sum_{i=1}^p \sum_{j=1}^q Y_{ij}} \quad j_g = \frac{\sum_{i=1}^p \sum_{j=1}^q j \times Y_{ij}}{\sum_{i=1}^p \sum_{j=1}^q Y_{ij}} \quad (8)$$

To achieve the scaling invariance, the NMI is given by dividing the mass of the binary image, i.e.,

$$\text{NMI} = \lambda = \frac{\sqrt{J_{i_g j_g}}}{m} \quad m = \sum_{i=1}^p \sum_{j=1}^q Y_{ij} \quad (9)$$

where m is the mass of the binary image and is equal to the sum of all the pixel values for the 2-D binary image Y_{ij} with size $p \times q$. Therefore, translation and rotation invariance is achieved by the moment of inertia for the binary image, and scaling invariance is achieved by dividing the mass of the binary image. These invariance properties of the NMI are helpful for object discrimination [24].

For the binary images of the u th block obtained by the PCNN model, i.e., $Y_1[u]$ and $Y_2[u]$, at different times, the corresponding NMI feature vectors, i.e., $\lambda_1[u] = \{\lambda_1[u][n], n = 1, \dots, N\}$ and $\lambda_2[u] = \{\lambda_2[u][n], n = 1, \dots, N\}$, are calculated when the iteration number n is changed from 1 to N , respectively. $\lambda_1 = \{\lambda_1[u], u = 1, \dots, U_X\}$ and $\lambda_2 = \{\lambda_2[u], u = 1, \dots, U_X\}$ represent the NMI feature vectors of the whole images at different times.

E. Change Detection Processing

For the NMI feature vectors of the u th block at different times, i.e., $\lambda_1[u]$ and $\lambda_2[u]$, the correlation coefficient between the NMI feature vectors, i.e., $\lambda_1[u]$ and $\lambda_2[u]$, is calculated as follows:

$$\rho_{\lambda_1[u]\lambda_2[u]} = \frac{\sum \lambda_1[u]\lambda_2[u] - \frac{\sum \lambda_1[u]\sum \lambda_2[u]}{N}}{\sqrt{\left(\sum \lambda_1[u]^2 - \frac{(\sum \lambda_1[u])^2}{N}\right) \left(\sum \lambda_2[u]^2 - \frac{(\sum \lambda_2[u])^2}{N}\right)}} \quad (10)$$

If the correlation coefficient is larger than an experiential value, e.g., 0.5, the block can be considered as an unchanged area. If not, the block is known as a hot spot area and is considered to be a changed area.

For the detected changed area (block), the EM algorithm [6] is utilized to obtain the final change map of the changed block using the original images at different times. Compared with the previous change detection algorithms based on the EM algorithm for a whole image, the proposed algorithm only uses the EM algorithm to process the hot spot changed area obtained by PCNN and NMI. As a result, the proposed algorithm can be used for very large remote sensing images.

F. Stopping Condition

This process repeats from *Step B* to *Step E* until all the blocks are processed. The final change map is the output.

III. EXPERIMENTS AND ANALYSIS

The aforementioned algorithm was coded in Visual C++ 6.0 and was tested on different HSR images. Comparisons between the proposed MPCNNCD algorithm and the traditional change detection algorithms of the change detection algorithm based on EM (EMCD) and the PCNNCD algorithm [11] were completed. An estimation of the change map accuracy for the various methods is provided.

A. Description of the Data Sets

In order to test the effectiveness of the proposed method, two multitemporal data sets were used. The first data set was obtained by QuickBird, with a spatial resolution of 0.6 m. The images (400×400 pixels) were acquired in 2002 and 2005 from Wuhan University, Wuhan, China, as shown in Fig. 4(a) and (b), respectively. The main land types are grass, road, and building. The ground truth of the change detection mask for the test area is shown in Fig. 4(c). The second data set (400×400 pixels, 0.6 m) was acquired by IKONOS in 2002 and 2004, as shown in Fig. 5(a) and (b). Its main land types are grass, road,

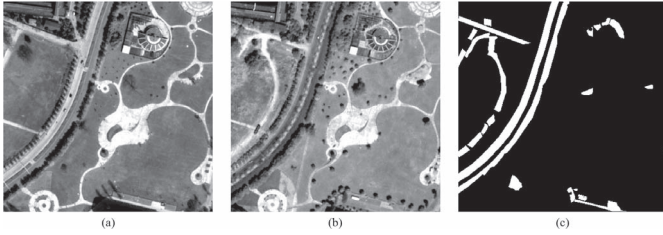


Fig. 4. QuickBird data set. (a) QuickBird image from 2002. (b) QuickBird image from 2005. (c) Ground truth mask.



Fig. 5. IKONOS data set. (a) IKONOS image from 2002. (b) IKONOS image from 2004. (c) Ground truth mask.

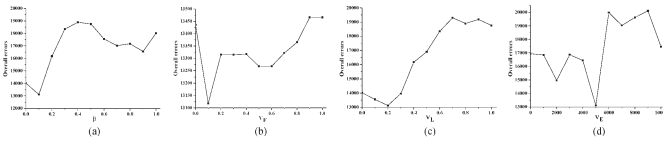


Fig. 6. Sensitivity analysis in relation to the parameters for the QuickBird imagery. (a) β . (b) V_F . (c) V_L . (d) V_E .

building, and water. The ground truth of the change detection mask for the test area is shown in Fig. 5(c), which distinguishes the changed and unchanged areas.

B. Design of the Experiments

In the two experiments, certain parameters have less impact on the change detection performance, so that they could be chosen as follows, based on experience. $\alpha_F = 0.1$, $\alpha_L = 1.0$, $\alpha_\theta = 1.0$, iteration number = 20, and the synaptic weight coefficients matrix $M = W = [0.707 \ 1 \ 0.701; 1 \ 1 \ 1; 0.707 \ 1 \ 0.707]$. For the other parameters, they were set based on a sensitivity test to tradeoff between missed alarms and overall errors. The sensitivity analysis using the QuickBird data is reported in Fig. 6, showing the relationship between the overall errors and each parameter. To analyze the sensitivity in relation to one of the parameters, the other parameters were set to be constant, as follows: $\beta = 0.1$, $V_F = 0.1$, $V_L = 0.2$, and $V_E = 5000$. The related parameters could then be selected in a certain range, as follows: β , V_F , and V_L were set from 0–1, with an interval of 0.1; and V_E was set from 0–10000, with an interval of 1000.

The other parameters were therefore selected based on the sensitivity test to tradeoff between missed alarms and overall errors, as follows. In the QuickBird experiment, $\beta = 0.1$, $V_F = 0.1$, $V_L = 0.2$, and $V_E = 5000$, whereas $\beta = 0.2$, $V_F = 0.2$, $V_L = 0.2$, and $V_E = 3000$ in the IKONOS experiment. Note that β was set to be 0.3 in the sensitivity analysis to obtain the minimum number of overall errors. The size of the blocks was set to 20×20 according to the size of the original image, and the overlap size was 4 for the 400×400 original image. In EMCD, the thresholds of change detection were 40 and 214, as obtained by the EM algorithm, for the two images, respectively.

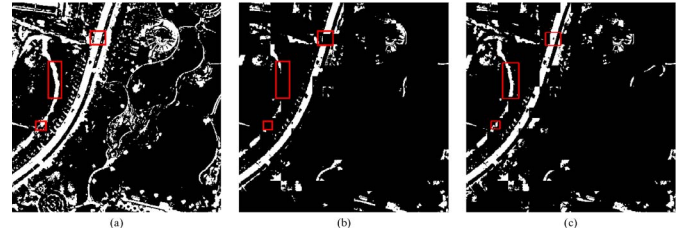


Fig. 7. Change detection results for the different methods with the QuickBird imagery. (a) EMCD. (b) PCNNCD. (c) MPCNNCD.

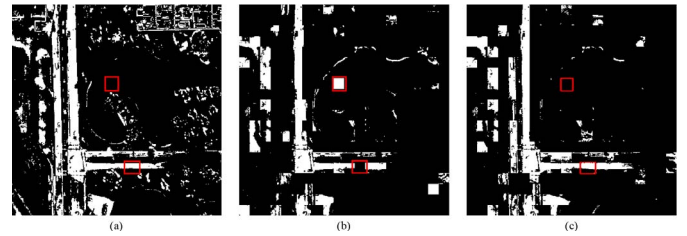


Fig. 8. Change detection results for the different methods with the IKONOS imagery. (a) EMCD. (b) PCNNCD. (c) MPCNNCD.

TABLE I
COMPARISONS OF THE DIFFERENT CHANGE DETECTION APPROACHES

Experiments	Algorithms	False alarms	Missed alarms	Overall errors
Experiment 1 QuickBird image	EMCD	19940	3545	23485
	PCNNCD	4094	9747	13841
	MPCNNCD	5212	7906	13118
Experiment 2 IKONOS image	EMCD	12286	9401	21687
	PCNNCD	6853	13076	19929
	MPCNNCD	6406	11024	17430

C. Experimental Results and Analysis

Figs. 7(a)–(c) and 8(a)–(c) show the change detection results by the use of EM, PCNNCD, and MPCNNCD for the QuickBird and IKONOS images, respectively. The visual comparisons of the three change detection algorithms show varying degrees of accuracy in pixel assignment. Compared with the ground truth mask in Figs. 4(c) and 5(c), PCNNCD and MPCNNCD have better visual change detection results and have fewer false changed areas. Compared with the PCNNCD results shown in Figs. 7 and 8, some of the improved change detection results for MPCNNCD for the changed areas are highlighted by red boxes, where it can be seen that PCNNCD lost these areas. As a result, MPCNNCD can achieve better visual accuracy not only in the changed areas but also in the unchanged areas.

To evaluate the classification performances of the different change detection algorithms, the overall change detection error, the number of false alarms, and the number of missed alarms are utilized. Table I demonstrates the results of the comparisons between the ground truth mask and the change detection results obtained by EM, PCNNCD, and MPCNNCD. The total number of changed pixels is 16 935 and 24 244 for the QuickBird and IKONOS images, respectively.

From Table I, it is apparent that PCNNCD and MPCNNCD, with fewer overall errors, produce better change detection results than the EM algorithm. This is because they are based on PCNN models that are combined with the spatial information.

To clearly describe the process of MPCNNCD, the intermediate results for the QuickBird image are reported in Fig. 9,

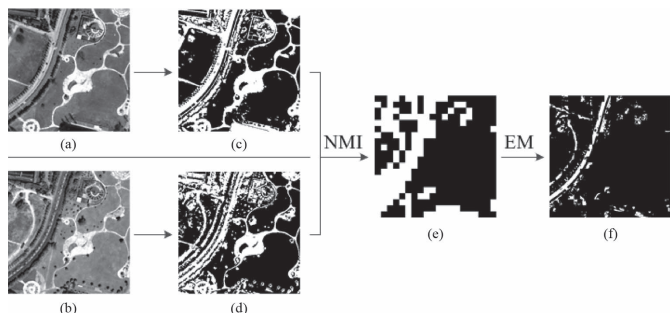


Fig. 9. Intermediate results of MPCNNCD for the QuickBird image.

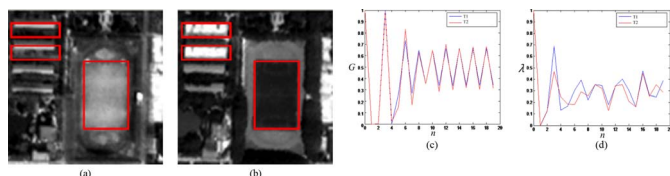


Fig. 10. Comparisons of the different change detection algorithms based on PCNN. (a) QuickBird block in 2002. (b) QuickBird block in 2005. (c) Feature image of PCNNCD [11]. (d) Feature image of MPCNNCD.

according to the flowchart of MPCNNCD. In the MPCNNCD algorithm, the binary image can be obtained using the PCNN model and the NMF feature to detect the hot spot changed areas. Finally, the EM algorithm is utilized to obtain the final change-detection-algorithm-based hot spot changed areas.

In addition, to describe the difference between the PCNNCD and MPCNNCD algorithms, a simple example is shown in Fig. 10, where three main changed areas in red boxes are noted. However, in the feature image of PCNNCD, the feature curves at different times are very similar; that is, they will be misclassified as an unchanged area. However, MPCNNCD can obtain the correct results when the feature curves are different. In addition, MPCNNCD utilizes the EM algorithm to obtain the final change map for the hot spot areas and provides more detailed information. As discussed in the experiments, these results demonstrate that MPCNNCD is a better change detection algorithm than the traditional PCNN change detection algorithms for HSR imagery.

IV. CONCLUSION

A modified change detection technique based on the PCNN model and the NMI feature, namely MPCNNCD, has been designed and implemented in this letter. The proposed algorithm utilizes the PCNN model to obtain the binary image, which can be combined with the spatial contextual information in the neighborhood of each pixel. The NMI feature is then used to detect the hot spot changed areas. In addition, MPCNNCD utilizes the EM algorithm to obtain a precise change map. Compared with the traditional change detection methods, the qualitative and quantitative results show that the proposed method produces fewer overall errors for both the QuickBird and IKONOS images. Consequently, MPCNNCD provides an effective option for HSR image change detection. In our future work, we will investigate how to automatically set the parameters for the method [17], and larger data sets will be processed.

REFERENCES

- [1] L. Bruzzone and F. Bovolo, "A novel framework for the design of change-detection systems for very-high-resolution remote sensing images," *Proc. IEEE*, vol. 101, no. 3, pp. 609–630, Mar. 2013.
- [2] Z. Yetgin, "Unsupervised change detection of satellite images using local gradual descent," *IEEE Trans. Geosci. Remote Sens.*, vol. 50, no. 5, pp. 1919–1929, May 2012.
- [3] L. Bruzzone and D. F. Prieto, "Automatic analysis of the difference image for unsupervised change detection," *IEEE Trans. Geosci. Remote Sens.*, vol. 38, no. 3, pp. 1171–1182, May 2000.
- [4] F. Bovolo and L. Bruzzone, "A theoretical framework for unsupervised change detection based on change vector analysis in the polar domain," *IEEE Trans. Geosci. Remote Sens.*, vol. 45, no. 1, pp. 218–236, Jan. 2007.
- [5] T. Celik, "Unsupervised change detection in satellite images using principal component analysis and *k*-means clustering," *IEEE Geosci. Remote Sens. Lett.*, vol. 6, no. 4, pp. 772–776, Oct. 2009.
- [6] A. P. Dempster, N. M. Laird, and D. B. Rubin, "Maximum likelihood from incomplete data via the EM algorithm," *J. R. Stat. Soc.*, vol. 39, no. 1, pp. 1–38, 1977.
- [7] M. Dalla Mura, J. A. Benediktsson, F. Bovolo, and L. Bruzzone, "An unsupervised technique based on morphological filters for change detection in very high resolution images," *IEEE Geosci. Remote Sens. Lett.*, vol. 5, no. 3, pp. 433–437, Jul. 2008.
- [8] M. N. Klaric *et al.*, "GeoCDX: An automated change detection and exploitation system for high-resolution satellite imagery," *IEEE Trans. Geosci. Remote Sens.*, vol. 51, no. 4, pp. 2067–2086, Apr. 2013.
- [9] S. Ghosh, L. Bruzzone, S. Patra, F. Bovolo, and A. Ghosh, "A context-sensitive technique for unsupervised change detection based on Hopfield-type neural networks," *IEEE Trans. Geosci. Remote Sens.*, vol. 45, no. 3, pp. 778–789, Mar. 2007.
- [10] F. Pacifici, F. Del Frate, C. Solimini, and W. J. Emery, "An innovative neural-net method to detect temporal changes in high-resolution optical satellite imagery," *IEEE Trans. Geosci. Remote Sens.*, vol. 45, no. 9, pp. 2940–2952, Sep. 2007.
- [11] F. Pacifici and F. Del Frate, "Automatic change detection in very high resolution images with pulse-coupled neural networks," *IEEE Geosci. Remote Sens. Lett.*, vol. 7, no. 1, pp. 58–62, Jan. 2010.
- [12] R. Eckhorn, H. J. Reitboeck, M. Arndt, and P. Dicke, "Feature linking via synchronization among distributed assemblies: Simulations of results from cat visual cortex," *Neural Comput.*, vol. 2, no. 3, pp. 293–307, Fall 1990.
- [13] J. L. Johnson, "Pulse-coupled neural nets: Translation, rotation, scale, distortion and intensity signal invariance for images," *Appl. Opt.*, vol. 33, no. 26, pp. 6239–6253, Sep. 1994.
- [14] J. L. Johnson and M. L. Padgett, "PCNN models and applications," *IEEE Trans. Neural Netw.*, vol. 10, no. 3, pp. 480–498, May 1999.
- [15] Z. Wang, Y. Ma, F. Cheng, and L. Yang, "Review of pulse-coupled neural networks," *Image Vis. Comput.*, vol. 28, no. 1, pp. 5–13, Jan. 2010.
- [16] T. Lindblad and J. M. Kinser, *Image Processing Using Pulse-Coupled Neural Networks*, 2nd ed. New York, NY, USA: Springer-Verlag, 2005.
- [17] Y. Chen, S.-K. Park, Y. Ma, and R. Ala, "A new automatic parameter setting method of a simplified PCNN for image segmentation," *IEEE Trans. Neural Netw.*, vol. 22, no. 6, pp. 880–892, Jun. 2011.
- [18] G. Kuntimad and H. S. Ranganath, "Perfect image segmentation using pulse coupled neural networks," *IEEE Trans. Neural Netw.*, vol. 10, no. 3, pp. 591–598, May 1999.
- [19] J. A. Karvonen, "Baltic Sea ice SAR segmentation and classification using modified pulse-coupled neural networks," *IEEE Trans. Geosci. Remote Sens.*, vol. 42, no. 7, pp. 1566–1574, Jul. 2004.
- [20] K. Zhan, H. Zhang, and Y. Ma, "New spiking cortical model for invariant texture retrieval and image processing," *IEEE Trans. Neural Netw.*, vol. 20, no. 12, pp. 1980–1986, Dec. 2009.
- [21] Z. Wang, Y. Ma, and J. Gu, "Multi-focus image fusion using PCNN," *Pattern Recognit.*, vol. 43, no. 6, pp. 2003–2016, Jun. 2010.
- [22] U. Ekblad and J. M. Kinser, "Theoretical foundation of the intersecting cortical model and its use for change detection of aircraft cars and nuclear explosion tests," *Signal Process.*, vol. 84, no. 7, pp. 1131–1146, Jul. 2004.
- [23] L. Zhang, Q. Yuan, H. Shen, and P. Li, "Multiframe image super-resolution adapted with local spatial information," *J. Opt. Soc. Amer. A.*, vol. 28, no. 3, pp. 281–390, Mar. 2011.
- [24] L. A. Torres-Mendez, J. C. Ruiz-Suarez, L. E. Sucar, and G. Gomez, "Translation, rotation, and scale-invariant object recognition," *IEEE Trans. Syst. Man, Cybern. C, Appl. Rev.*, vol. 30, no. 1, pp. 125–130, Feb. 2000.